RSC Advances

PAPER

View Article Online
View Journal | View Issue

Cite this: *RSC Adv.*, 2022, **12**, 12453

Electronic, mechanical, optical and piezoelectric properties of glass-like sodium silicate (Na_2SiO_3) under compressive pressure

R. Zosiamliana,[ab] Lalrinkima,[ab] B. Chettri,[ac] G. Abdurakhmanov,[de] M. P. Ghimire[f] and D. P. Rai*[a]

The structural, mechanical, electronic, optical and piezoelectric properties of Na_2SiO_3 are studied under varying compressive unidirectional pressure (0–50 GPa with a difference of 10 GPa) using density functional theory (DFT). The calculated structural properties agree well with previously reported results. At 12 GPa, our calculation shows a structural phase transition from orthorhombic $Cmc2_1$ to triclinic $P1$. The mechanical profile of Na_2SiO_3 structures under different compressive unidirectional pressures are analysed by calculating the elastic moduli, Poisson's ratio and eigenvalues of stiffness matrix. Our study shows the mechanical stability of the system up to a pressure of 40 GPa. Herein, we have obtained an indirect band gap of 2.97 eV at 0 GPa. Between 0–50 GPa, the band gaps are within the range 2.62 to 3.46 eV. The system in our study possesses a wide band gap and high optical absorption in the UV-Vis range of electromagnetic radiation. The calculated static refractive indices $\eta^{x,y,z}(0)$ are close to unity suggesting its transparency. For piezoelectric properties, we have reported the total Cartesian polarization. Our calculations have revealed that Na_2SiO_3 is a promising candidate for optoelectronic devices while its application in ferroelectric and piezoelectric devices could be improved with further research.

Received 20th February 2022
Accepted 31st March 2022

DOI: 10.1039/d2ra01125e

rsc.li/rsc-advances

1 Introduction

Theoretical and experimental insight into novel silica (SiO_2) based glasses have become an interesting topic among researchers due to their wide-direct bandgap, high thermodynamic stability, low thermal conductivity and abundance in nature.[1,2] Their flexibility and reliability towards different applications for different tasks has made them one of the most promising candidates for technological and commercial applications, such as battery and storage systems, fireproof fabrics, fiber optics, bio-active glasses for antibiotic-free antibacterial materials, optoelectronic devices, *etc.*[3–7] Moreover, modifying such properties during the manufacturing process can enhance the resistivity towards thermal, chemical or pressure inputs, plus they are transparent, making silicate glasses promising materials over a wide range of applications.[8–11] Most of the important glasses are silicate glass, based on the compound silica (SiO_2) or quartz.[12] The structure of silicate glass was thought to be well understood at a local level. Randall *et al.*[13] have performed experimental investigations using X-ray diffraction and reported that the vitreous silica probably consists of small crystals of cristobalite.[13] A later study on silica (SiO_2) by Zachariasen *et al.*[14] reported that the heat-treated specimens occurred in vitreous forms and showed relative tetrahedral orientation with two neighbouring oxygens. It has also been reported that silicon atoms surrounded by oxygen may vary within a wide limit, as the oxygen to oxygen bond angle varies throughout the whole network.[14,15] This leads to more considerations while investigating the structure of silicate glass.

Pure silica is a three dimensional network of [SiO_4] tetrahedrally arranged in a way that the silicon atom is bonded to four neighbouring oxygen atoms and in turn each oxygen atom is bonded to two silicon atoms.[16] The structure is well described by the continuous random network (CRN).[14] The addition of alkali Na^+ cations disrupts the Si–O–Si bridging bonds (BO) and results in the formation of non-bridging oxygen (NBO) consisting of one half of the permanent broken oxygen bond. The Na^+ ions sit close to the NBO forming weak ionic bonds producing the formation of glass-like sodium metasilicate ($SiO_2 + Na_2O \rightarrow Na_2SiO_3$, $\Delta H^{773K} = -235$ kJ mol^{-1}).[17,18] Alkali silicates are the most studied glass materials due to their important chemical and physical properties which make them

[a]*Department of Physics, Physical Sciences Research Center (PSRC), Pachhunga University College, Mizoram University, Aizawl-796001, India. E-mail: dibya@pucollege.edu.in*

[b]*Department of Physics, Mizoram University, Aizawl-796004, India*

[c]*Department of Physics, North-Eastern Hill University, Shillong-793022, Meghalaya, India*

[d]*Tashkent State Technical University, Tashkent, 100095, Uzbekistan*

[e]*National University of Uzbekistan, Tashkent, 100174, Uzbekistan*

[f]*Central Department of Physics, Tribhuvan University, Kirtipur 44613, Kathmandu, Nepal. E-mail: madhav.ghimire@cdp.tu.edu.np*

relevant materials in science and technology. A few decades ago, the structure, mechanical and electronic properties of glass-like sodium silicate (Na_2SiO_3) started being investigated through experimental as well as computational simulation methods. In the pioneering work of Grund and Pizy,[19] they investigated the structure of Na_2SiO_3 and the atomic positions were determined by Patterson and Fourier–Bragg projections,[20] which noted that the structure showed pseudo-hexagonal symmetry (as later refined by Richet *et al.*[21] *via* Raman spectroscopy and X-ray diffraction). Later, an experimental investigation using single-energy Raman spectroscopy and energy-dispersive X-ray powder diffraction revealed a structural phase transition from the orthorhombic $Cmc2_1$ (space group) to the lower primitive symmetry space group at 850 K.[21]

Experimentally, different techniques and approaches have been implemented: Raman spectroscopy, X-ray diffraction (XRD), nuclear magnetic resonance (NMR), X-ray absorption fine structure and extended X-ray absorption fine structure (XAFS and EXAFS) are the most common experimental set-ups for structural determination and property studies.[22–31] However, Na_2SiO_3 lacks long-range order (LRO) or transitional periodicity that causes complications, making it much more challenging to study the structural properties than for other crystalline solids.[32] To generate useful data and necessary information, reverse Monte Carlo and *Ab Initio* Molecular Dynamics (AIMD) based on density functional theory (DFT) are the most useful simulation methods.[33–35] Computational DFT-based AIMD has accurate inter-atomic potential and has become the major appliance to probe the details of amorphous solids, where the structure is generally controlled by short-range order (SRO) and medium range order (MRO).[36]

As far as we are aware, among the surveyed literature the theoretical and the experimental work is mainly focused on the structural and electronic properties of Na_2SiO_3. So, in this work in addition to the structural and electronic properties of Na_2SiO_3, we have also emphasised the unexplored properties like phase-transition, optical and piezoelectric properties under different unidirectional compressive pressures within the framework of DFT.

2 Computational details

All calculations were performed using density functional theory. A linear combination of the atomic orbital method (LCAO) employed in QuantumATK Q-2019.12 was adopted for all DFT calculations.[37–39] For all electrons, an exchange-correlation functional of generalized gradient approximation (GGA) within the Perdew–Burke–Ernzerhof (PBE) scheme is adopted.[40] Our sodium silicate unit cell consists of 24 atoms with 8-sodium, 4-silicon and 12-oxygen atoms. The space group of the $Na_8Si_4O_{12}$ is $Cmc2_1$ or C_{2v}^{12}. We have employed the force field method with limited-memory Broyden–Fletcher–Goldfarb–Shanno (LBFGS) algorithm coupled with the ReaxFF_CHO-SiNa_2018 and Pedone_LiNaKSiO_2007 potentials for geometry optimization.[41–43] These force field potentials are specially designed for alkali silicates and commonly used for their property calculations. The minimum criteria for Hellmann–Feynman force and stress tolerance were set to 0.01 eV $Å^{-1}$ and 0.0001 eV $Å^{-3}$, respectively, for geometry optimization. During geometry optimization, no constraints were imposed on the structure along any axes. The pseudopotential of Na, Si and O considering the medium basis set (similar to double zeta polarized) is used for our calculation.[44] The density mesh cut off was set to 125.0 Ha. The self-consistent field (SCF) tolerance was set to 10^{-5} Ha. The above mentioned geometry convergence criteria were followed for all structures under a compressive stress of 0–50 GPa with a difference of 10 GPa. The Monkhorst–Pack method was used to sample the *K*-points[45] within a first Brillouin zone. For all the electronic property calculations $5 \times 3 \times 6$ *K*-points were sampled. Moreover, for the partial density of states and optical calculations a high *k*-mesh of $8 \times 5 \times 10$ was taken into consideration.

3 Results and discussion

3.1 Structural properties

In this section, we discuss the structural properties of the Na_2SiO_3. The unit cell of $Na_8Si_4O_{12}$ exists as an orthorhombic crystal structure with space group $Cmc2_1$. It is to be noted that for the convenience of our calculation we have swapped the *x* and *z* axis ($a \leftrightarrow c$) and applied the unidirectional compressive pressure along the longer axis (*z*-axis). The optimised lattice parameters are $a = 6.158$ Å, $b = 4.876$ Å, $c = 10.630$ Å. The optimised volume (V) of the unit cell is found to be 319.20 $Å^3$. The optimised lattice parameters (a, b, c in Å unit) *versus* energy (in eV) are presented in Fig. 1. Table 1 shows the agreement between our results and the previously calculated results from Cuautli *et al.*[46] using PBE as the exchange-correlation functional. Our calculated volume is 2.04% and 3.95% higher than the volume calculated using the Becke, 3-parameter, Lee–Yang–Parr (B3LYP) functional by Belmonte *et al.*[47] and the one experimentally obtained by McDonald *et al.*,[48] respectively. The difference in volume is due to the well-known effect of the generalized gradient approximation (GGA) exchange-correlation functional by PBE.

The change in lattice parameters under unidirectional compressive pressure in the pressure range 0 → 50 GPa are reported in Table 2. The current work gives a thorough study of the structural deformation under the unidirectional compressive pressure (0–50 GPa). However, we do not have sufficient experimental or theoretical data to compare the results of pressure related studies for Na_2SiO_3. With the increase in pressure, the negative deformation along the lattice constant 'Δc' and the positive one along 'Δa' and 'Δb', indicates compression and tensile strain, respectively (see Table 2). On application of compressive pressure the change in lattice parameter '*c*' is high as compared to '*a*' and '*b*' due to the unconstrained *x* and *y*-axes as a result of the dissipation of tensile stress along the *x*- and *y*-axes. This specifies that our compressive pressure is unidirectional acting along the lattice parameter '*c*'. The structural deformations at different pressures led to a change in the optimised unit cell volume as: at $P = 0, 10, 20, 30, 40, 50$ (in GPa), $V = 319.2, 328.5, 319.4, 311, 305.1, 301.6$ (in $Å^3$), respectively.

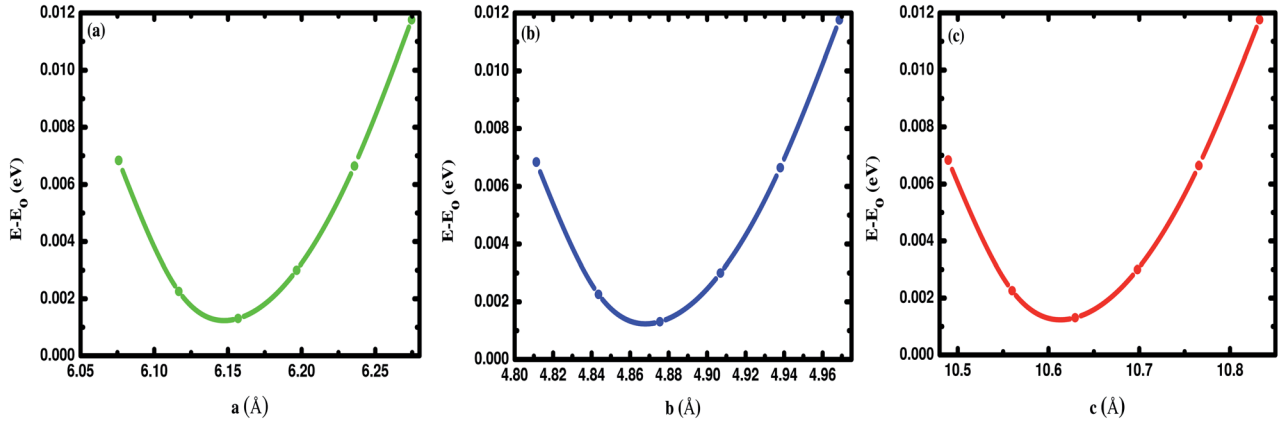

Fig. 1 Difference in energy ($E-E_0$) in eV as a function of the lattice constants of Na_2SiO_3 (a) a (Å), (b) b (Å) and (c) c (Å). E_0 indicates the minimum ground state energy.

Table 1 Calculated optimised lattice parameters of Na_2SiO_3 compared to B3LYP (Belmonte *et al.*[47]), PBE (Cuautli *et al.*[46]) and experimental (McDonald *et al.*[48]) results [swapped x and z axis ($a \leftrightarrow c$)]

Parameters	PBE–GGA (this work)	B3LYP[47]	PBE[46]	Exp.[48]
a (Å)	6.158	6.0977	6.16	6.07
b (Å)	4.876	4.8523	4.88	4.82
c (Å)	10.630	10.5676	10.63	10.48
V (Å^3)	319.20	312.673	319.546	306.6

Table 2 Calculated lattice parameters in Å and the change in lattice parameters with respect to the pristine cell in Å under different unidirectional pressure in GPa [swapped x and z axis ($a \leftrightarrow c$)]

P	a	b	c	Δa	Δb	Δc
0	6.158	4.876	10.630	0	0	0
10	6.157	5.221	10.22	−0.001	0.345	−0.41
12	6.198	5.233	10.08	0.040	0.357	−0.55
20	6.326	5.276	9.569	0.168	0.400	−1.061
30	6.446	5.316	9.077	0.288	0.440	−1.553
40	6.531	5.348	8.736	0.373	0.472	−1.894
50	6.588	5.388	8.497	0.430	0.512	−2.133

The hallmarks of the Na_2SiO_3 structure are the presence of [SiO_4] tetrahedral chains and the existence of BO and the NBO bonds where the sodium atoms are attached. The presence of NBOs in the structure make a large distortion on the tetrahedral [SiO_4] units.[18] Initially, at 0 GPa pressure, our Na_2SiO_3 exists as an orthorhombic crystal structure with space group $Cmc2_1$. As shown in Fig. 2, Na_2SiO_3 experiences a structural phase transition from the orthorhombic $Cmc2_1$ space group to the lower primitive symmetry of a triclinic crystal structure with space group $P1$ at 12 GPa.

3.2 Mechanical properties

This section is about the mechanical properties of Na_2SiO_3. In order to perceive whether our compound meets the required stability and durability for practical applications, knowledge of its mechanical and elastic properties are essential. We have calculated the elastic constants and other mechanical properties for Na_2SiO_3 under different compressive unidirectional pressure. Our calculated elastic constants (as shown in Table 3) and the elastic constants calculated by Belmonte *et al.*[47] (using LCAO DFT/B3LYP functionals) are different due to the difference in the exchange-correlation functionals employed. However, the two results satisfy the necessary and sufficient Born criteria of mechanical stability for an orthorhombic system:[49]

$$\begin{gathered} C_{11}>0,\quad C_{11}C_{22}>C_{12}{}^2, \\ \left[C_{11}C_{22}C_{33}+2C_{12}C_{13}C_{23}-C_{11}C_{23}{}^2-C_{22}C_{13}{}^2-C_{33}C_{12}{}^2\right]>0, \\ C_{44}>0,\quad C_{55}>0,\quad C_{66}>0 \end{gathered} \tag{1}$$

From Table 3, it can be seen that the stability criteria for the orthorhombic system are satisfied at 0 and 10 GPa pressure showing the mechanical stability of the orthorhombic phase of Na_2SiO_3. In the previous sub-section, we have reported that there is a phase transition from orthorhombic $Cmc2_1$ to triclinic $P1$ at 12 GPa pressure. Further, for the triclinic system the Born criteria of mechanical stability are:[49,50]

$$\begin{gathered} C_{11}>0, C_{22}>0, C_{33}>0, C_{44}>0, C_{55}>0, C_{66}>0, \\ \left[C_{11}+C_{22}+C_{33}+2(C_{12}+C_{13}+C_{23})\right]>0, C_{33}C_{55}-C_{35}{}^2>0, \\ C_{44}C_{66}-C_{46}{}^2>0, C_{22}+C_{33}-2C_{23}>0 \end{gathered} \tag{2}$$

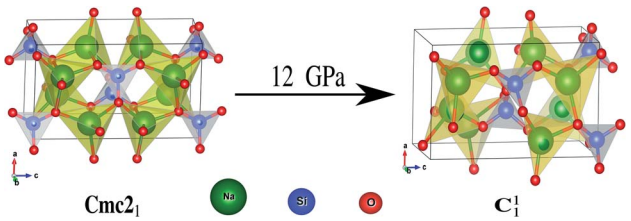

Fig. 2 Phase transition from $Cmc2_1 \rightarrow C_1^1$ under 12 GPa unidirectional compressive pressure.

Table 3 Calculated elastic constants C_{ij} under different unidirectional pressure (both in GPa units). Here, at 0 and 10 GPa Na_2SiO_3 is in the orthorhombic ($Cmc2_1$) phase and between 12–50 GPa Na_2SiO_3 is in the triclinic ($P1$) phase

P	C_{11}	C_{22}	C_{33}	C_{44}	C_{55}	C_{66}	C_{12}	C_{13}	C_{23}	C_{35}	C_{46}	C_{15}	C_{25}
0	57.36	43.76	59.70	24.32	51.91	27.74	43.47	19.38	10.51	—	—	—	—
10	52.60	157.37	111.47	38.05	21.60	50.56	29.81	34.62	42.08	—	—	—	—
12	45.27	154.18	135.71	36.35	26.58	48.35	34.21	43.54	53.20	−11.11	−9.94	−5.28	−6.08
20	80.36	179.37	188.73	27.41	18.38	55.80	53.81	45.66	60.86	−2.28	−2.62	−8.08	−4.58
30	118.92	189.26	196.31	20.92	16.46	59.71	71.84	58.66	62.90	1.24	−1.68	−2.48	−0.31
40	131.05	180.53	207.47	17.47	16.62	62.87	71.60	66.00	68.26	0.36	−0.82	−2.66	−1.47
50	5.25	180.28	169.59	22.00	30.47	53.31	19.14	41.27	57.20	5.05	5.32	−28.00	−13.01

Our calculated elastic constants in the pressure range 12–50 GPa (as shown in Table 3) satisfy the above-mentioned mechanical stability criteria for the triclinic phase of Na_2SiO_3. The agreement of the stability criteria show that our system for Na_2SiO_3 is mechanically stable at the different compressive pressure ranges, 0–50 GPa. This is also confirmed by the fact that the stiffness matrix is positive at all pressures except at $P =$ 50 GPa as can be seen in the eigenvalues reported in Table 5. At 50 GPa there is a mismatch between the Born criteria for mechanical stability and the stiffness matrix eigenvalues where we get a negative value at λ_1. Mouhat *et al.*[49] reported that when studying low-symmetry crystals like monoclinic and triclinic, it was usually more convenient to keep the stiffness coefficients in the matrix form and check whether all eigenvalues of C were positive. In Fig. 3, we present the calculated phonon dispersion curves of Na_2SiO_3 to test its dynamical stability between 0–50 GPa. Since, the unit cell consists of 24 atoms, there are 72 branches in the phonon dispersion curve. At 0 and 30 GPa [see Fig. 3(a and d)] we observe positive phonon spectra, this implies that Na_2SiO_3 is dynamically stable at these pressures. However, at 10, 20, 40 and 50 GPa [see Fig. 3(b, c, e and f)] we obtain small negative phonon spectra which could just be numerical noise in the calculation, as the lowest phonon curve does not cross the energy value of −10 meV in any of the four cases. This implies that the considered system *i.e.*, Na_2SiO_3 is dynamically stable between the applied mechanical stress of 0–50 GPa. From Table 3, it is obvious that between $P =$ 10–40 GPa our calculated C_{11}, C_{22}, C_{33} are considerably larger than C_{66}, C_{55}, C_{44} which shows that Na_2SiO_3 has more resistance to axial compression as compared to shear deformation. This can be confirmed by comparing the bulk modulus and shear modulus reported in Table 4. From the analysis of our calculated elastic constants (C_{ij}), it can be seen that C_{11} and C_{22} decreases while C_{55} increases when pressure escalates from 10 GPa to 12 GPa, this suggests that there is a tendency of phase transition from orthorhombic $Cmc2_1$ to the lower symmetry phase (see Fig. 2).

In Table 4, the calculated elastic moduli and the Poisson's ratio under different compressive pressures are reported. Our reported bulk modulus (B), Young's modulus (Y) and shear modulus (G) are estimated in Voigt (uniform strain assumption),[51] Reuss (uniform stress assumption)[52] and Hill assumption.[53] It can be seen that there are regular or small fluctuations in our calculated elastic moduli from 0–40 GPa pressures indicating that our system is mechanically stable. At $P =$ 50 GPa, the elastic moduli fluctuate very high or our calculated elastic moduli are out of order compared to lower pressures (*i.e.* 0–40 GPa), which might be due to the fact that our system (Na_2SiO_3) shows mechanical instability at 50 GPa. Glass-like Na_2SiO_3 materials are usually brittle.[54] The brittleness or ductility is generally characterized by the values of Poisson's ratio. We have reported our calculated Poisson's ratio (ν) estimated using the

Table 5 Calculated eigenvalues of stiffness matrix (in GPa units) calculated from elastic constants under different unidirectional pressures

P	λ_1	λ_2	λ_3	λ_4	λ_5	λ_6
0	5.7103	19.843	28.63	47.31	50.672	112.62
10	16.694	32.253	41.275	54.111	90.336	196.98
12	23.039	25.862	32.821	54.016	93.228	217.47
20	16.984	27.313	54.458	56.227	123.93	271.14
30	15.739	20.84	60.16	70.957	131.56	302.32
40	15.909	17.629	63.062	77.369	127.3	314.75
50	−20.633	21.085	44.627	54.416	120.81	240.59

Table 4 Calculated elastic moduli (bulk modulus (B), Young's modulus (Y), and shear modulus (G) all in GPa) and Poisson's ratio (ν) (unitless) under varying unidirectional pressure (in GPa units). Here, the subscripts V, R and H represent Voigt, Reuss and Hill assumptions, respectively

P	B_V	B_R	B_H	Y_V	Y_R	Y_H	G_V	G_R	G_H	ν_V	ν_R	ν_H
0	34.171	26.067	30.119	63.406	27.146	45.921	26.625	10.233	18.429	0.19074	0.32643	0.24589
10	59.384	41.197	50.291	90.613	67.677	79.168	36.371	27.596	31.983	0.24569	0.22621	0.23763
12	66.34	42.744	54.542	91.177	67.057	79.182	35.87	27.071	31.471	0.27094	0.23853	0.25804
20	85.458	68.677	77.068	102.74	79.334	91.042	39.527	30.339	34.933	0.29963	0.30747	0.30311
30	99.032	93.485	96.259	106.13	79.365	92.894	40.157	29.21	34.684	0.32139	0.35851	0.33916
40	103.42	99.311	101.37	106.93	77.512	92.424	40.271	28.291	34.281	0.32767	0.36992	0.34803
50	65.593	−118.29	−26.349	93.411	601.82	−5549.5	36.99	128.16	82.574	0.26265	1.34790	−34.603

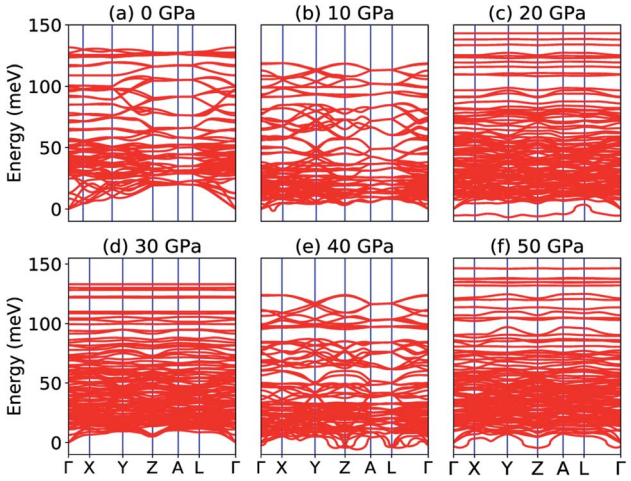

Fig. 3 Phonon dispersion curve of Na_2SiO_3 under (a) 0 GPa, (b) 10 GPa, (c) 20 GPa, (d) 30 GPa, (e) 40 GPa, (f) 50 GPa.

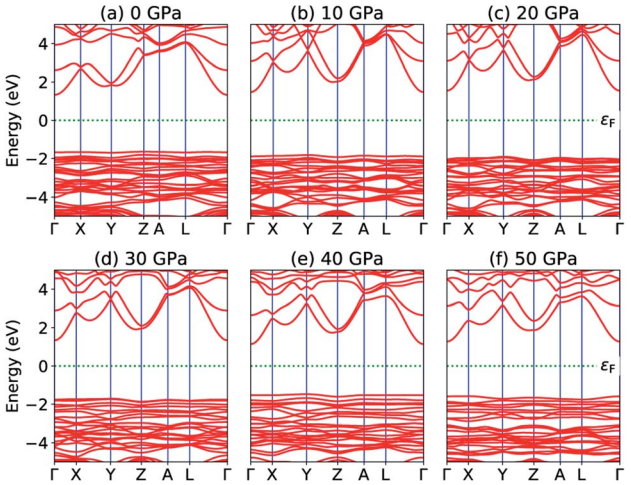

Fig. 4 Calculated band structure (a) $P = 0$ GPa, (b) $P = 10$ GPa, (c) $P = 20$ GPa, (d) $P = 30$ GPa, (e) $P = 40$ GPa and (e) $P = 50$ GPa.

Voigt, Reuss and Hill assumptions. From Table 4, it is obvious that the value of ν increases with pressure showing that Na_2SiO_3 becomes more ductile with pressure. Interestingly, between 0–40 GPa, one can find that our system undergoes tensile deformation which can be confirmed by the fact that all the Poisson's ratios are positive in this range of pressure. However, at 50 GPa, the value of ν_H falls drastically to become negative. This negative Poisson's ratio (at $\nu_H = -34.603$, see Table 4) results in compressive deformation. Thus, at 50 GPa, Na_2SiO_3 shows auxetic material properties which have wide applications possibilities in biomedical field, surgical implants and even for piezoelectric sensors and actuators.[55–58]

3.3 Electronic properties

The most fundamental property while investigating atomic level interactions in any material is the electronic property. In this section, we present detailed results of the electronic properties of pristine Na_2SiO_3 (0 Gpa) and Na_2SiO_3 at five different pressures. Fig. 4 and 5 show the calculated electronic band structures and partial density of states (PDOS) for Na_2SiO_3, respectively. It is found that the top of the valence bands (VBs) have small dispersions while the bottom of the conduction bands (CBs) have large dispersions for all different compressive pressures (see Fig. 4). This is in good agreement with the electronic band structure result reported by Lui *et al.*[59] using *ab initio* total-energy and force calculations within the local density approximation (LDA) *via* a preconditioned conjugate gradient algorithm. From our calculation, at $P = 0$ GPa [see Fig. 4(a)], the highest energy of the valence band is at the Z point, and the lowest energy of the conduction band is at the Γ point, and with an indirect (Z to Γ points) band gap of 2.97 eV. Experimentally, Sigel[60] reported a band gap of 6 eV for silicate glasses. It is well known that PBE–GGA density functional theory calculations usually underestimate the band gap. An indirect (Z to Γ points) band gap was reported by Lui *et al.*[59] but with a band gap value of 4 eV. Ching *et al.*[18] reported band gap values of 6.46 eV with $\alpha = \frac{2}{3}$ and 9.98 eV with $\alpha = 1.0$ and concluded that the band gap of Na_2SiO_3 is very dependent on the exchange parameter used. In this work, we have done electronic band structure calculations under compressive pressures in the pressure range 0–50 GPa with a difference of 10 GPa. It is found that the highest energy point of the valence band changes with pressure while the bottom of the conduction band is at Γ point at each pressure, see Fig. 4(a–f). It is obvious that the application of pressure changes the lattice parameters and so the average distance between electron or hole. This in turn changes the magnitude of the electron–hole ion potential. This change in the potential is significant as it plays an important role in determining the band gap at the Brillouin zone. In this work, we have found that the band gap fluctuates with the application of pressure. Initially, the band gap increases up to 20 GPa, and from 20–40 GPa the band gap decreases linearly. From 40–50 GPa, the band gap starts to increase again (see Fig. 6 for

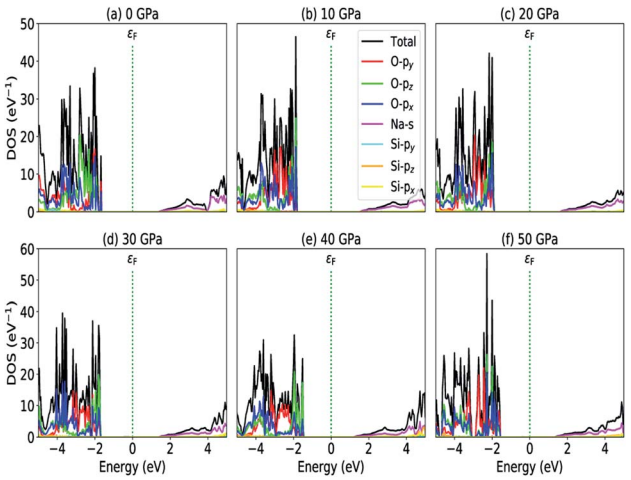

Fig. 5 Partial density of states (a) $P = 0$ GPa, (b) $P = 10$ GPa, (c) $P = 20$ GPa, (d) $P = 30$ GPa, (e) $P = 40$ GPa and (e) $P = 50$ GPa.

variation of band gap with the application of pressure). Obviously, the band gap should decrease with increasing applied pressure but, from our calculation, we can clarify that the variation in band gap with the application of pressure does not follow a specific trend (*i.e.*, there is a rise and fall in the band gap value when the amount of applied pressure increases). This might be due to the nature of the material being investigating.

The calculated PDOS of Na_2SiO_3 at 0 GPa, 10 GPa, 20 GPa, 30 GPa, 40 GPa and 50 GPa are shown in Fig. 5 (a)–(f), respectively. The Fermi level (ε_F) is set at 0 eV which lies between the valence band and the conduction band. At 0 GPa, the energy states around the top of the valence band are mainly contributed by the states O-2p_x and O-2p_y orbitals. And, the valence band electronic states are mainly distributed in the energy range from −3.8 eV to −1.8 eV owing to the hybridization of O-2p_x, O-2p_y, O-2p_z and Si-3p_x. The energy states around the bottom of the conduction band are composed mainly of the Na-3s orbitals and also, we could find a slight contribution from Si-3p_x orbitals. With the application of pressure, the main contributors of the energy state at the top of the valence band changes *i.e.*, from the state O-2p_y to O-2p_z until it reaches 40 GPa [see Fig. 5(b, c, d and e)] while, the energy states which contributed the bottom of the conduction band remains consistent. Clearly, we could find an overall shift of both the valence band and conduction band when pressure increases. At 10 and 20 GPa both the top of the valence band and the bottom of the conduction band shift away from the Fermi level (ε_F). Therefore, the band gap is large, and hence, light of a higher frequency and lower wavelength would be absorbed. Between 30–50 GPa, we observed the reverse characteristic where both the top of the valence band and the bottom of the conduction band shift towards the Fermi level (ε_F). As a result, there is a reduction in band gap and therefore light absorption in the visible range might be improved.

3.4 Optical properties

The optical properties of a material define how the material interacts with electromagnetic radiation.[61] So, a detailed study of the optical properties is crucial in many industrial and scientific applications such as heat transfer, contactless temperature measurement, laser technology, optics industry for the productions of mirrors, lenses and optical windows, photovoltaic industry, the aerospace industry and so on.[62,63] Therefore, we have studied the optical properties of Na_2SiO_3 at different compressive pressures by calculating the dielectric constant (ε), absorption coefficient (α) and refractive index (η) as a function of the photon energy (eV). We have calculated the optical properties of Na_2SiO_3 in terms of complex dielectric function which is closely related to the interaction between the photons (electromagnetic radiation) and the electrons (atoms), therefore it is represented by both the real and the imaginary parts given by:[64–67]

$$\varepsilon = \varepsilon_1 + i\varepsilon_2 \tag{3}$$

where ε_1 and ε_2 are the real part and imaginary part of the dielectric constant, respectively. The above equation is mainly connected with the electronic structures and determines the linear response of the material to electromagnetic radiation. The imaginary part (ε_2) is related to the electronic band and represents the optical absorption in the crystal and is given by:[64–67]

$$\varepsilon_2(\omega) = \frac{\hbar^2 e^2}{\pi m^2 \omega^2} \sum_{nn'} \int_k d^3k \left| \left\langle \vec{k}n \middle| \vec{p} \middle| \vec{k}n' \right\rangle \right|^2 \times \left[1 - f\left(\vec{k}n\right)\right] \delta\left(E_{\vec{k}n} - E'_{\vec{k}n} - \hbar\omega\right) \tag{4}$$

where $\vec{p}$ is the momentum operator, $|\vec{k}n\rangle$ is the eigenfunction of the eigenvalue $E_{\vec{k}n}$ and $f(\vec{k}n)$ is the Fermi distribution function. The real part (ε_1) is evaluated from the imaginary part (ε_2) using the Kramers–Kronig transformation[68] which is given by:

$$\varepsilon_1(\omega) = 1 + \frac{2}{\pi} \int_0^\infty \frac{\varepsilon_2(\omega')\omega' d\omega'}{\omega'^2 - \omega^2} \tag{5}$$

The optical constant, the refractive index (η) can be computed from the complex dielectric function (ε_1). The absorption coefficient (α) and the refractive index (η) which are the optical properties related to the dielectric function and are given by:

$$\alpha(\omega) = \frac{2\omega\kappa(\omega)}{c} \tag{6}$$

where $\kappa(\omega)$ is the extinction coefficient related to the imaginary part of the complex refractive index.

$$\eta(\omega) = \sqrt{\frac{(\varepsilon_1{}^2 + \varepsilon_2{}^2)^{\frac{1}{2}} + \varepsilon_1}{2}} \tag{7}$$

The presence of discrete spikes in the electronic density of states influences the optical properties. The real part (ε_1) and imaginary part (ε_2) of the dielectric constant as a function of the photon energy up to 10 eV along the *x*, *y*, *z*-axes under $P = 0$, 10, 20, 30, 40, 50 GPa's are presented in Fig. 7(a and b). The calculated static real dielectric function $\varepsilon_1(0)$ (at $E = 0.0$ eV) along the *x*, *y*, *z*-axes are presented in Table 6. The real dielectric function ε_1 shows anisotropic behaviour up to 10 eV, beyond 10 eV the values of ε_1 are ~1 arb. unit under different applied pressures along different axes

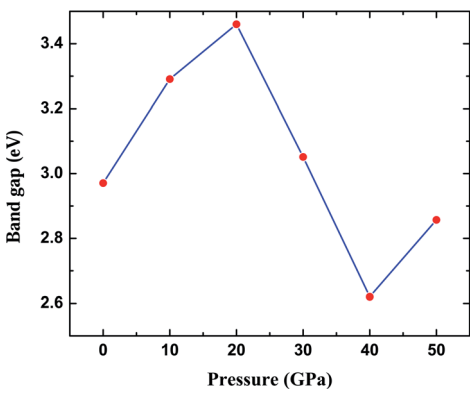

Fig. 6 Calculated band gap (in eV) *versus* pressure (in GPa) for Na_2SiO_3. Here, the red dots represent the corresponding band gaps at 0, 10, 20, 30, 40, 50 GPa.

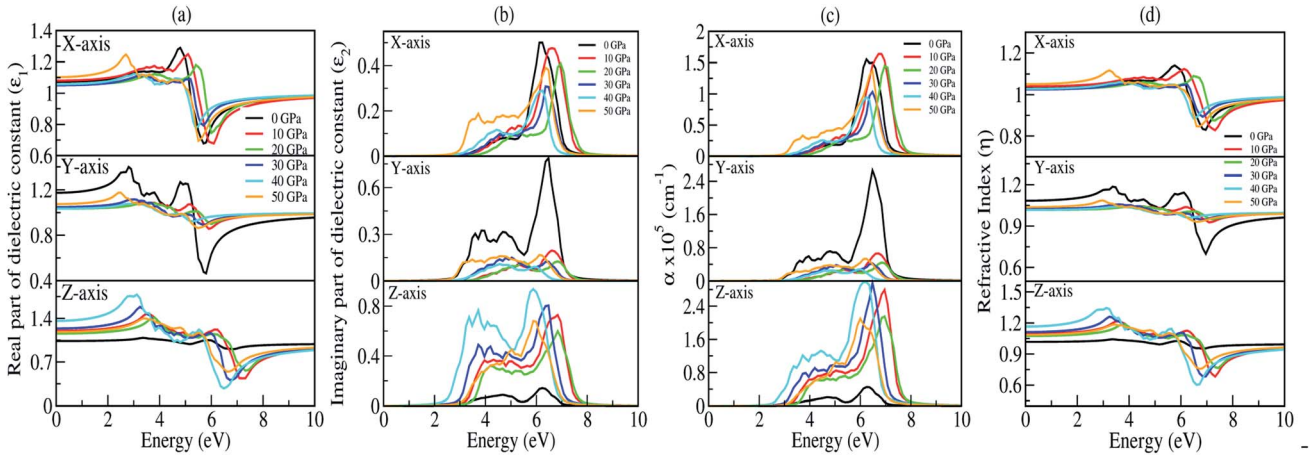

Fig. 7 Optical parameters as a function of the photon energy (in eV) under 0, 10, 20, 30, 40, and 50 GPa pressures: (a) real part of the dielectric function (ε_1), (b) imaginary part of the dielectric function (ε_2), (c) absorption coefficient (α) and (d) refractive index (η).

exhibiting negligible effects of pressure on the ε_1 for high values of photon energy. Meanwhile, along the *x*-axis one could find one prominent peak for each different pressure, as shown in Fig. 7(a) (top). For 0 GPa the peak point is at around 5.0 eV with a value of 1.3 arb. unit. The peak points shifted to the higher energy region as pressure increases until it reaches 20 GPa, and from 30 GPa the peak points shift back to the lower energy region until the pressure reaches 50 GPa where the peak point is at around 2.85 eV with a peak value of 1.24 arb. unit. The value of ${\varepsilon_1}^x$ goes to a lower value after reaching the maximum point. The minimum points for all different pressures are in the energy region where the photon energy is at 5–6.2 eV with the minimum value in the range of 0.65–0.80 arb. unit. However, along the *y*-axis, as shown in Fig. 7(a) (middle), we note two prominent peak points for 0 GPa where the first peak is at around 2.85 eV and the second peak is at around 4.8 eV with peak values of ~1.4 and ~1.3 arb. unit, respectively, and as the photon energy is increasing ${\varepsilon_1}^y$ drops below 0.5 arb. unit at around 6 eV. The peak value as well as the lowest value of ${\varepsilon_1}^y$ at 0 GPa are comparatively high and low, respectively, when comparing with the peak value and the lowest value at all other pressures being applied within the same energy range. This indicates that along the *y*-axis, the photon energy might have the greatest effect on the refractive index when the pressure is at 0 GPa. Considering the second peak, one can note that ${\varepsilon_1}^y$ shows similar behaviour as that in the case of ${\varepsilon_1}^x$ where the peak points shift to the higher photon energy region and go back to the lower photon energy when pressure is increased. Along the *z*-axis, as shown in Fig. 7(a) (bottom), the value of ${\varepsilon_1}^z$ at 0 GPa almost remains the same throughout the energy range, it has a maximum peak value at around 6 eV with a value of ~1.05 arb. unit. As pressure increases the peak points are shifted to the lower energy region within the energy range 3.0–4.0 eV. At 40 GPa one could find the highest peak for this axis which is at around 3.0 eV with a value of ~1.75 arb. unit.

The imaginary part of the dielectric constant ε_2 is interconnected with the dielectric loss, and also corresponds to the inter-band transition between the valence band and conduction band. It is highly correlated with the optical absorption (α) of a material [see Fig. 7(c)]. Plot of the imaginary part of the dielectric constant (ε_2) as a function of the photon is shown in Fig. 7(b). Along the *x* and *y*-axes, one can note that the peak points of ${\varepsilon_2}^x$ and ${\varepsilon_2}^y$ [see Fig. 7(b) (top and middle)] are shifted to the higher photon energy region when pressure increases, until the pressure reaches 20 GPa but above this the peak points shift back towards the lower energy region which is very similar to the one we obtained in the real part. However, when analyzing our calculated data for ε_2 along the *z*-axis, it clearly shows that within the same energy range the ${\varepsilon_2}^z$ has a much higher value when comparing with ${\varepsilon_2}^x$ and ${\varepsilon_2}^y$, except at 0 GPa. This is due to the fact that the pressure is applied along the *z*-axis. We have measured absorption coefficients (α) along the *x*, *y*, *z*-axes as a function of incident photon energy as shown in Fig. 7(c). Here, we can see very strong optical absorption along the *x*, *y*, *z*-axes (α^x, α^y, α^z) under different pressures within the energy range 0–10 eV. The most active region is found between 2.5 eV to 8.0 eV. The absorption spectra is highly anisotropic in nature. Our main concern is to observe the variation of absorption spectra under the applied pressure for its potential application in opto-electronic devices. Our results of absorption spectra are very interesting because they fall within the UV-Vis range. Referring to Fig. 7(c) (bottom), the absorption spectra peaks show a blue shift up to 20 GPa pressure, after which there is a small red shift as compared to the one at 0 GPa. The intensity of absorption spectra increases as we keep increasing the pressure up to 40 GPa. The minimum threshold energy is found to be 2.5 eV which

Table 6 Calculated static real part of the dielectric constant $\varepsilon_1(0)$ and static refractive indices $\eta(0)$ along the *x*, *y*, *z*-axes under 0, 10, 20, 30, 40 and 50 GPa pressures

P	${\varepsilon_1}^x(0)$	${\varepsilon_1}^y(0)$	${\varepsilon_1}^z(0)$	$\eta^x(0)$	$\eta^y(0)$	$\eta^z(0)$
0	1.07	1.18	1.04	1.03	1.08	1.01
10	1.08	1.04	1.20	1.04	1.02	1.09
20	1.05	1.03	1.16	1.02	1.01	1.07
30	1.05	1.05	1.24	1.02	1.02	1.10
40	1.06	1.03	1.36	1.02	1.01	1.16
50	1.11	1.08	1.18	1.05	1.03	1.08

corresponds to an optical band gap in good agreement with the electronic band gap at 40 GPa [Fig. 7(c) (bottom)]. We have observed four prominent peaks at 3.2 eV, 3.8 eV, 4.5 eV and 6 eV. The optical band gap is a result of the first direct electron transition from the top of the valence band (O-p_z) to the bottom of the conduction band (Na-s) along Γ-symmetry. The first peak at 3.2 eV is a result of the transition from the third band of the valence region to the bottom of the conduction band (Γ-symmetry). The second peak at 3.8 eV is a probability transition from the top of the valence band to the bottom of the conduction band along the *z*-symmetry point. The third peak at 4.5 eV is due to the outcome of the transition from the second band of the valence region to the first band of the conduction region along the *x*-symmetry point. The last peak at 6 eV having maximum intensity, is due to a transition from the third band of the valence region to the third band of the conduction region along the *x*-symmetry point. Interestingly, the maximum intensity peaks shift towards higher energy with increasing pressure for the *x*- and *y*-axes which is contrary to the absorption spectra peak measured along the *z*-axis. This discrepancy is due to the tensile strain along the *x*- and *y*-axes while the compressive strain is experienced by the atom along the *z*-axis on application of unidirectional pressure (along the *z*-axis).

The calculated spectra of refractive indices (η) along the *x*, *y*, *z*-axes are presented in Fig. 7(d). The static refractive indices $\eta_{x,y,z}(0)$ are given in Table 6. Clearly, all the values are close to unity at 0 eV indicating that our system Na_2Si0_3, is transparent in nature. Recently, Baral *et al.*[69] reported the high refractive index of $(Na_2O)_x$ $(SiO_2)_{1-x}$ when sodium oxide concentration is increased. Using the orthogonal linear combination of atomic orbitals (OLCAO) method in the VASP-relaxed structures he reported an η value in the range of 1.415–1.530 when the concentration was x = 0–0.5. On analysing the variation of refractive indices (η) with respect to the incident photon energy (eV) under unidirectional pressure along the *z*-axis, one can find the change in refractive index is almost negligible along the *x*- and *y*-axes up to around 5.5 eV even when the pressure reaches 50 GPa [see Fig. 7(d) (top and middle)]. However, referring to Fig. 7(d) (bottom), along the *z*-axis we note isotropic behaviour. The refractive indices start increasing at around 3 eV as pressure escalates compared to at 0 GPa where the value almost remains at unity throughout the whole incident photon energy. Meanwhile, above 6 eV the values of all the refractive indices (*i.e.*, along *x*, *y*, *z*) falls below 1 up to around 10 eV [see Fig. 7(d)]. This seems physically impossible as a refractive index of below 1 occurs only when the speed of light is exceeded by phase velocity of an electromagnetic wave ($v_p > c$). In addition, this phenomenon arises due to the presence of plasmonic vibration.

3.5 Piezoelectric properties

It is well-known that the piezoelectric properties of a material arises as a result of the atomic scale polarization which could be due to the application of mechanical stress.[70] The study of piezoelectric properties of a material has become an interesting topic among researchers as those materials have industrial applications – as actuators, sensors, microphones and so on – also they have applications in medical devices for monitoring heartbeats and breathing.[71–78] To our knowledge this insight study of piezoelectric properties of a material are usually based on the study of piezoelectric tensors ($\boldsymbol{d}_{kij}$).[79,80] Interestingly, in this section we are going to discuss the piezoelectric properties of glass-like Na_2SiO_3 by calculating the total Cartesian polarization under different compressive unidirectional pressure as shown in Table 7. Our calculations are simply based on modern theory of polarization where the spontaneous polarization of a material is calculated to understand its ferroelectric properties. Since quartz (SiO_2) is a naturally occurring single crystalline piezoelectric material, our system of Na_2SiO_3 has the possibility of showing piezoelectric properties. In modern theory of polarization, polarization of a material is divided into two parts; electronic and ionic. The contribution of the electronic part to polarization is given as:[81]

$$P_e = \frac{-2|e|i}{(2\pi)^3}\int_A \mathrm{d}k_\perp \sum_{n=1}^{M}\int_0^{G_\parallel} \langle U_{k,n}| \frac{\partial}{\partial k_\parallel} |U_{k,n}\rangle \mathrm{d}k_\parallel \quad (8)$$

Here, the summation runs over occupied bands, and $k_\parallel$ is parallel to the direction of polarization, and $G_\parallel$ is a reciprocal lattice vector in the same direction. The states $|U_{k,n}\rangle$ are the cell-periodic parts of the Bloch functions, $\psi_{k,n} = U_{n,k}(r)\, e^{ik.r}$.

The electronic polarization part is simply calculated by the classical electrostatic sum of point charges given as:

$$P_i = \frac{|e|}{\Omega}\sum_\nu Z_{ion}{}^\nu r^\nu \quad (9)$$

where the summation runs over all the ions in the unit cell, and $Z_{ion}{}^\nu$ and r^ν are the valence charge and position vector of atom ν, and Ω is the unit cell.

The total Cartesian polarization ($P_t(c)$) is calculated by taking the product of total fractional polarization (P_t) and polarization quantum (P_q), *i.e.*,

$$P_t(c) = P_t P_q \quad (10)$$

where $P_t = P_e + P_i$ is the sum of electronic and ionic polarization parts and $P_q{}^j = \frac{|e|R^j}{\Omega}$ is the polarization quantum, here, $|e|$ is the electronic charge, R^j is the lattice vector, $\boldsymbol{j}$ and Ω the unit cell volume.

Our calculated total Cartesian polarization in cm^{-2} under different compressive unidirectional pressures are given in Table 7. From our calculations, one can see that at 0 GPa the Cartesian polarization is maximum along the *z*-direction with a value of ~ 0.1 cm^{-2}. This indicates that Na_2SiO_3 shows some ferroelectric properties. However, when pressure is applied along the *z*-axis, it is obvious that one will notice compressive stress along the *z*-axis with tensile stress observed along both the *x*- and *y*-axes. This structural change with pressure will patently distort the negative cloud of electrons around the positive atomic nuclei. This slight separation will result in an electric field between them, and consequently polarization is created which can be manipulated to give novel piezoelectric properties. Our biggest concern is to obtain the Cartesian polarization of Na_2SiO_3 for its potential application in piezoelectric materials. Interestingly, from Table 7 we have observed

Table 7 Calculated total Cartesian polarization $P_t(c)$ in cm^{-2} along the *x*, *y*, *z*-axes under different compressive unidirectional pressures

P	0	10	20	30	40	50
x	$-2.97064990 \times 10^{-3}$	$-2.66488487 \times 10^{-2}$	$2.36226850 \times 10^{-2}$	$-7.18990850 \times 10^{-3}$	$-9.0549006 \times 10^{-3}$	$1.77675552 \times 10^{-2}$
y	$-2.29594955 \times 10^{-2}$	$4.11457135 \times 10^{-2}$	$6.31891403 \times 10^{-2}$	$7.57134265 \times 10^{-2}$	$6.49859613 \times 10^{-2}$	$-6.33370486 \times 10^{-2}$
z	$1.00901047 \times 10^{-1}$	$1.64564653 \times 10^{-2}$	$8.47809484 \times 10^{-3}$	$-5.85834073 \times 10^{-3}$	$-3.35035488 \times 10^{-3}$	$1.39032451 \times 10^{-3}$

that the maximum polarization axis changes from *z* to *y*-axes as pressure increases from 0 GPa to 40 GPa. At 50 GPa the Cartesian polarization has its highest value along the *x*-axis. The calculated Cartesian polarization for 10, 20, 30, 40 and 50 GPa are $\sim$ 0.041, 0.063, 0.076, 0.065 and 0.018 (in cm^{-2}) which are fairly low. Therefore, to use Na_2SiO_3 in practical ferroelectric and piezoelectric devices, rigorous research is necessary which could further enhance its polarizability.

4 Conclusions

In summary, we have studied the properties of Na_2SiO_3 using DFT calculations under varying unidirectional compressive pressure. Our findings reveal that Na_2SiO_3 is a stable structure which shows mechanical stability up to 40 GPa. And at 12 GPa, our system experiences a structural phase transition from orthorhombic $Cmc2_1$ to a lower primitive symmetry triclinic *P*1 structure. Also, at 50 GPa Na_2SiO_3 is found to be an auxetic material which opens up its potential application in the field of biomedical and other electronic devices. Interestingly, Na_2SiO_3 is also found to have its optical absorbance within the UV-Vis range. The value of $\eta^{x,y,z}(0)$ $\sim$1 has revealed that Na_2SiO_3 is transparent in nature. Therefore, it is a promising material for optoelectronic devices.

Conflicts of interest

There are no conflicts to declare.

Acknowledgements

D. P. Rai acknowledges the Government of India, Ministry of Science and Technology, Department of Science & Technology (International Bilateral Cooperation Division) for supporting the Indo-Uzbek joint project via Sanction No. INT/UZBEK/P-02. M.P.G. acknowledges the Alexander von Humboldt Foundation, Germany, for the equipment grants; and IFW-Dresden, Germany, for providing the large-scale computing hardware to Tribhuvan University for the scientific computations.

References

1 L.-g. Liu, *Geophys. Res. Lett.*, 1987, **14**, 1079–1082.
2 J. M. D. Coey, *Mössbauer Spectroscopy Applied to Inorganic Chemistry*, Springer US, Boston, MA, 1984, pp. 443–509.
3 L. Zhu, Y. R. Zeng, J. Wen, L. Li and T. M. Cheng, *Electrochim. Acta*, 2018, **292**, 190–198.
4 Y. Ren, Y. Zhang, Y. Gu and Q. Zeng, *Prog. Org. Coat.*, 2017, **112**, 225–233.
5 M. Lancry, E. Régnier and B. Poumellec, *Prog. Mater. Sci.*, 2012, **57**, 63–94.
6 S. Kaya, M. Cresswell and A. R. Boccaccini, *Mater. Sci. Eng. C*, 2018, **83**, 99–107.
7 E. Borsella, E. Cattaruzza, G. De Marchi, F. Gonella, G. Mattei, P. Mazzoldi, A. Quaranta, G. Battaglin and R. Polloni, *J. Non-Cryst. Solids*, 1999, **245**, 122–128.
8 J. O. Bockris, J. D. Mackenzie and J. A. Kitchener, *Trans. Faraday Soc.*, 1955, **51**, 1734.
9 C. A. Faick and A. N. Finn, *J. Am. Ceram. Soc.*, 1931, **14**, 518–528.
10 L. Shartsis, S. Spinner and W. Capps, *J. Am. Ceram. Soc.*, 1952, **35**, 155–160.
11 T. Uchino, M. Iwasaki, T. Sakka and Y. Ogata, *J. Phys. Chem.*, 1991, **95**, 5455–5462.
12 A. K. Varshneya and J. C. Mauro, *Fundam. Inorg. Glas.*, 2019, 1–18.
13 J. T. Randall, H. P. Rooksby and B. S. Cooper, *Z. Kristallogr. Cryst. Mater.*, 1930, **75**, 196–214.
14 W. H. Zachariasen, *J. Am. Chem. Soc.*, 1932, **54**, 3841–3851.
15 I. Farnan, *Nature*, 1997, **390**, 14–15.
16 K. Baral, A. Li and W.-Y. Ching, *J. Phys. Chem. A*, 2017, **121**, 7697–7708.
17 S. Kikuchi, N. Koga, H. Seino and S. Ohno, *J. Nucl. Sci. Technol.*, 2016, **53**, 682–691.
18 W. Y. Ching, R. A. Murray, D. J. Lam and B. W. Veal, *Phys. Rev. B*, 1983, **28**, 4724–4735.
19 A. Grund and M. Pizy, *Acta Crystallogr.*, 1952, **5**, 837–840.
20 D. D. Le Pevelen, *Encycl. Spectrosc. Spectrom.*, 2010, 2559–2576.
21 P. Richet, B. O. Mysen and D. Andrault, *Phys. Chem. Miner.*, 1996, **23**, 157–172.
22 G. Greaves, *J. Non-Cryst. Solids*, 1985, **71**, 203–217.
23 Y. Cao, A. N. Cormack, A. G. Clare, B. Bachra, A. C. Wright, R. N. Sinclair and A. C. Hannon, *J. Non-Cryst. Solids*, 1994, **177**, 317–323.
24 D. W. Matson, S. K. Sharma and J. A. Philpotts, *J. Non-Cryst. Solids*, 1983, **58**, 323–352.
25 H. Maekawa, T. Maekawa, K. Kawamura and T. Yokokawa, *J. Non-Cryst. Solids*, 1991, **127**, 53–64.
26 G. N. Greaves, S. J. Gurman, C. R. A. Catlow, A. V. Chadwick, S. Houde-Walter, C. M. B. Henderson and B. R. Dobson, *Philos. Mag. A*, 1991, **64**, 1059–1072.
27 M. G. Mortuza, R. Dupree and D. Holland, *J. Non-Cryst. Solids*, 2001, **281**, 108–116.
28 L. Olivier, X. Yuan, A. N. Cormack and C. Jäger, *J. Non-Cryst. Solids*, 2001, 53–66.
29 A. Meyer, J. Horbach, W. Kob, F. Kargl and H. Schober, *Phys. Rev. Lett.*, 2004, **93**, 027801.
30 B. Gee and H. Eckert, *J. Phys. Chem.*, 1996, **100**, 3705–3712.

31 G. N. Greaves, A. Fontaine, P. Lagarde, D. Raoux and S. J. Gurman, *Nature*, 1981, **293**, 611–616.
32 Y. Kowada and D. E. Ellis, *Adv. Quantum Chem.*, 1998, **29**, 233–251.
33 A. Bunde, M. Ingram, P. Maass and K. Ngai, *J. Non-Cryst. Solids*, 1991, **131–133**, 1109–1112.
34 R. L. McGreevy and L. Pusztai, *Mol. Simul.*, 1988, **1**, 359–367.
35 S. Ispas, M. Benoit, P. Jund and R. Jullien, *Phys. Rev. B*, 2001, **64**, 214206.
36 Z. Q. Hu, A. M. Wang and H. F. Zhang, *Mod. Inorg. Synth. Chem.*, 2017, 641–667.
37 S. Smidstrup, T. Markussen, P. Vancraeyveld, J. Wellendorff, J. Schneider, T. Gunst, B. Verstichel, D. Stradi, P. A. Khomyakov, U. G. Vej-Hansen, M.-E. Lee, S. T. Chill, F. Rasmussen, G. Penazzi, F. Corsetti, A. Ojanperä, K. Jensen, M. L. N. Palsgaard, U. Martinez, A. Blom, M. Brandbyge and K. Stokbro, *J. Phys. Condens. Matter*, 2020, **32**, 015901.
38 S. Smidstrup, D. Stradi, J. Wellendorff, P. A. Khomyakov, U. G. Vej-Hansen, M.-E. Lee, T. Ghosh, E. Jónsson, H. Jónsson and K. Stokbro, *Phys. Rev. B*, 2017, **96**, 195309.
39 M. Schlipf and F. Gygi, *Comput. Phys. Commun.*, 2015, **196**, 36–44.
40 J. P. Perdew, K. Burke and M. Ernzerhof, *Phys. Rev. Lett.*, 1996, **77**, 3865–3868.
41 D. C. Liu and J. Nocedal, *Math. Program.*, 1989, **45**, 503–528.
42 S. H. Hahn, J. Rimsza, L. Criscenti, W. Sun, L. Deng, J. Du, T. Liang, S. B. Sinnott and A. C. T. van Duin, *J. Phys. Chem. C*, 2018, **122**, 19613–19624.
43 A. Pedone, G. Malavasi, A. N. Cormack, U. Segre and M. C. Menziani, *Chem. Mater.*, 2007, **19**, 3144–3154.
44 M. van Setten, M. Giantomassi, E. Bousquet, M. Verstraete, D. Hamann, X. Gonze and G.-M. Rignanese, *Comput. Phys. Commun.*, 2018, **226**, 39–54.
45 H. J. Monkhorst and J. D. Pack, *Phys. Rev. B*, 1976, **13**, 5188–5192.
46 C. Cuautli, I. Romero-Ibarra, J. Vazquez-Arenas and M. Galvan, *Fuel*, 2021, **298**, 120840.
47 D. Belmonte, C. Gatti, G. Ottonello, P. Richet and M. V. Zuccolini, *J. Phys. Chem. A*, 2016, **120**, 8881–8895.
48 W. S. McDonald and D. W. J. Cruickshank, *Acta Crystallogr.*, 1967, **22**, 37–43.
49 F. Mouhat and F.-X. Coudert, *Phys. Rev. B*, 2014, **90**, 224104.
50 Q. Guo, K. C. Lau and R. Pandey, *J. Phys. Chem. C*, 2019, **123**, 4674–4681.
51 W. Voigt, *Lehrbuch der Kristallphysik*. Teubner Verlag, Leipzig, 1928. References - Scientific Research Publishing.
52 A. Reuss, *Z. Angew. Math. Mech.*, 1929, **9**, 49–58.
53 R. Hill, *Proc. Phys. Soc. Sect. A*, 1952, **65**, 349–354.
54 S. Chokka and K. Traipanya, *Suranaree J. Sci. Technol.*, 2017, **24**, 407–414.
55 M. Sanami, PhD thesis, Institute for Materials Research and Innovation, University of Bolton, Deane Road, Bolton BL3 5AB, UK, 2015.
56 E. P. Hadjigeorgiou and G. E. Stavroulakis, *Comput. Methods Sci. Technol.*, 2004, **10**, 147–160.
57 S. Farhangdoust, S. M. Aghaei, M. Amirahmadi, N. Pala and A. Mehrabi, *Sensors Smart Struct. Technol. Civil, Mech. Aerosp. Syst.*, 2020, **2020**, 36.
58 T. Fey, F. Eichhorn, G. Han, K. Ebert, M. Wegener, A. Roosen, K. I. Kakimoto and P. Greil, *Smart Mater. Struct.*, 2015, **25**, 015017.
59 F. Liu, S. H. Garofalini, R. D. King-Smith and D. Vanderbilt, *Chem. Phys. Lett.*, 1993, **215**, 401–404.
60 G. H. SIGEL, *TREATISE Mater. Sci. Technol.*, ACAdemic Press, INC., 1977, vol. 12, pp. 5–89.
61 V. Sudarsan, *Funct. Mater.*, 2012, 285–322.
62 L. Barnett, *Dev. Agric. Eng.*, 1986, **8**, 48–55.
63 A. K. Varshneya and J. C. Mauro, *Dev. Agric. Eng.*, 1986, **8**, 48–55.
64 C. Ambrosch-Draxl and J. O. Sofo, *Comput. Phys. Commun.*, 2006, **175**, 1–14.
65 D. P. Rai, T. V. Vu, A. Laref, M. P. Ghimire, P. K. Patra and S. Srivastava, *Nano-Struct. Nano-Objects*, 2020, **21**, 100404.
66 B. Chettri, P. K. Patra, L. Lalhriatzuala, S. Verma, B. K. Rao, M. L. Verma, V. Thakur, N. Kumar, N. N. Hieu and D. P. Rai, *Int. J. Quantum Chem.*, 2021, **121**, e26680.
67 B. Chettri, P. K. Patra, T. V. Vu, C. Q. Nguyen, Lalrinkima, A. Yaya, K. O. Obodo, N. T. T. Tran, A. Laref and D. P. Rai, *Phys. E*, 2021, **126**, 114436.
68 P. C. Martin, *Phys. Rev.*, 1967, **161**, 143–155.
69 K. Baral and W.-Y. Ching, *J. Appl. Phys.*, 2017, **121**, 245103.
70 Y. J. Lu, Z. F. Shi, C. X. Shan and D. Z. Shen, *Nanoscale Semicond. Lasers*, 2019, 75–108.
71 D. Damjanovic and R. E. Newnham, *J. Intell. Mater. Syst. Struct.*, 1992, **3**, 190–208.
72 J. Nuffer and T. Bein, *Glob. Symp. Innov. Solut. Adv. Transp. Ind.*, 2006, 4–6.
73 E. Aksel and J. L. Jones, *Advances in lead-free piezoelectric materials for sensors and actuators*, 2010.
74 M. T. Chorsi, E. J. Curry, H. T. Chorsi, R. Das, J. Baroody, P. K. Purohit, H. Ilies and T. D. Nguyen, *Adv. Mater.*, 2019, **31**, 1802084.
75 G. Gautschi, *Piezoelectric Sensorics*, Springer Berlin Heidelberg, Berlin, Heidelberg, 2002, pp. 73–91.
76 S. Zhang and F. Yu, *J. Am. Ceram. Soc.*, 2011, **94**, 3153–3170.
77 Y. Y. Chiu, W. Y. Lin, H. Y. Wang, S. B. Huang and M. H. Wu, *Sens. Actuators, A*, 2013, **189**, 328–334.
78 A. Zaszczyńska, A. Gradys and P. Sajkiewicz, *Polymers*, 2020, **12**, 2754.
79 P. Labéguerie, M. Harb, I. Baraille and M. Rérat, *Phys. Rev. B: Condens. Matter Mater. Phys.*, 2010, **81**, 045107.
80 X. Meng, X. Wen and G. Qin, *Comput. Mater. Sci.*, 2010, S372–S377.
81 R. D. King-Smith and D. Vanderbilt, *Phys. Rev. B: Condens. Matter Mater. Phys.*, 1993, **47**, 1651–1654.